

## **Solution-Based Integration of Vertically Stacked Organic Photodetectors Toward Easy-To-Fabricate Filterless Multi-Color Light Sensors**

*Ting Zhao, Kai Xia, Dario Natali, Vincenzo Pecunia\**

T. Zhao, K. Xia

Jiangsu Key Laboratory for Carbon-Based Functional Materials & Devices, Institute of Functional Nano & Soft Materials, Joint International Research Laboratory of Carbon-Based Functional Materials and Devices, Soochow University, China

Prof. D. Natali

Department of Electronics, Information and Bioengineering, Politecnico di Milano, P.za L. da Vinci, 32 Milan, 20133 Italy

and

Center for Nano Science and Technology @Polimi, Istituto Italiano di Tecnologia, Via Pascoli 70/3, I-20133 Milano, Italy

Prof. V. Pecunia

School of Sustainable Energy Engineering, Simon Fraser University, 5118 - 10285 University Drive, Surrey, V3T 0N1, BC, Canada

E-mail: [vincenzo\\_pecunia@sfu.ca](mailto:vincenzo_pecunia@sfu.ca)

**Keywords:** organic photodetectors, narrowband photodetectors, color sensing, vertically stacked photodetectors, Foveon-like architecture

### **Abstract**

Solution-processed, color-selective organic photodetectors are uniquely positioned to deliver high-performance, low-cost, multicolor light sensors/imagers beyond the limitations of conventional, color-filter-based technologies. To realize such potential, however, a prominent challenge has been the solution-based, monolithic integration of vertically stacked organic photodetectors, which would enable multicolor sensing with optimum light collection while

benefiting from the scalability, cost, and sustainability edges of solution-based manufacturing. To tackle this challenge, this paper demonstrates, for the first time, the monolithic integration of vertically stacked solution-processed organic photodetectors for independent, multicolor light sensing within the same pixel area. The solvent orthogonality challenge is tackled by selecting polymer-based photoactive layers and an insulating polymeric spacer—for independent biasing and photocurrent readout—with compatible processing conditions. Based on the suitable characteristics of blue- and green-sensitive standalone devices, the vertically stacked, monolithic device architecture is optimized by also incorporating semitransparent electrodes for photons to reach deep into the stack. The resultant device architecture enables efficient blue- and green-selective photodetection with state-of-the-art linearity, alongside speed of response adequate for real-world applications. Based on its solution-processability and modularity, this approach paves the way for the facile, solution-based fabrication of organic imagers covering multiple spectral regions with high sensitivity and resolution.

## 1. Introduction

Multicolor photodetection is key to a wide range of applications, not only in the conventional areas of colorimetry and digital photography, but also in emerging domains such as smart manufacturing, smart agriculture, smart homes, medical diagnostics, and wearable electronics.<sup>[1–6]</sup> Conventional photodetector technologies rely on semiconductors that have broadband absorption properties (e.g., silicon), which therefore require input optical filtering to achieve color selectivity.<sup>[2,7]</sup> This approach is exemplified by the adoption of imager architectures featuring a color filter array atop a matching broadband photodetector array<sup>[8]</sup> (**Figure 1a**). In such architectures, each pixel consists of several photodetectors laterally sharing the pixel area and underlying different color filters, with the signals from such photodetectors being interpolated to determine the color coordinates at that pixel. While commercially successful, this approach comes with important performance limitations. In addition to color artifacts, the fractioning of each pixel into a subset of photodetectors introduces conspicuous optical losses (on top of those associated with the non-ideal transmittance of the color filters), which impacts the imager performance and resolution.<sup>[8]</sup> For instance, in conventional red-green-blue imagers with four color filters per pixel, on average approximately two-thirds of the light is absorbed by the color filters (**Figure 1a**), thereby not contributing to light sensing. If multispectral imaging were to be pursued with this same approach, the optical losses would become even more severe, making this approach unsuitable.

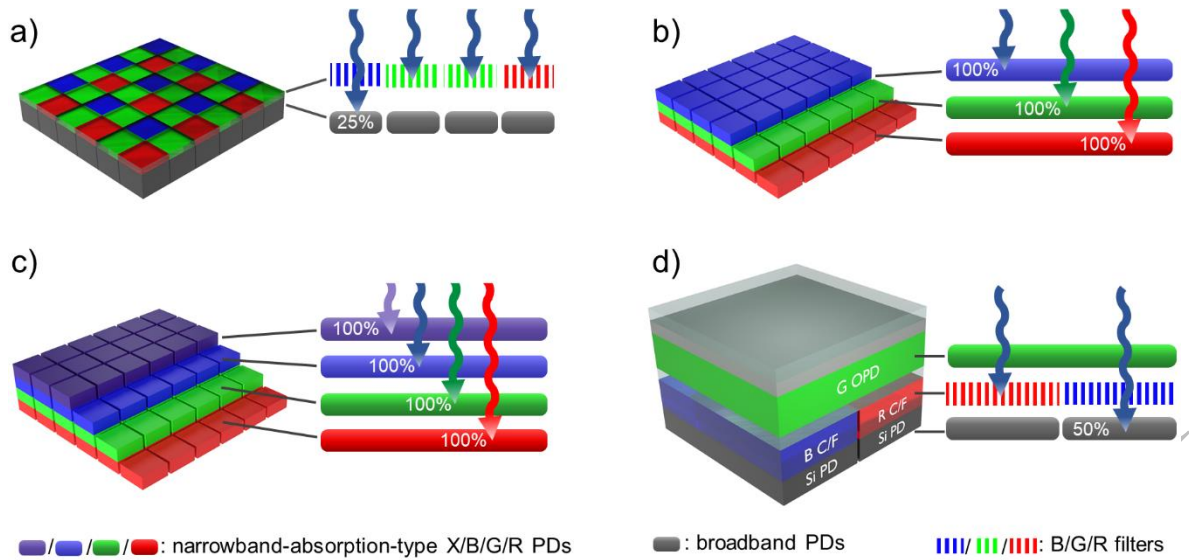


**Figure 1.** Impact of vertical photodetector stacking on color sensing. a) Conventional approach to color sensing based on a color filter array and broadband photodetectors: architecture (left) and schematic of the inherent dissipation of up to 75% of the light in the optical filters at each pixel (right). b) Vertically stacked filterless color sensors: architecture (left) and schematic of the capability of this approach to ultimately deliver zero optical losses (right). c) Potential of vertically stacked filterless color sensors for multispectral sensing by adding additional photodetectors in the stack sensitive to different spectral regions: architecture (left) and schematic of the capability of this approach to ultimately deliver zero optical losses (right). d) Hybrid color sensor featuring green selective photodetectors atop photodetectors equipped with color filters for red and blue light: architecture (left) and schematic of the inherent dissipation of up to 50% of the light in the optical filters at each pixel (right). Legend: B = blue; G = green; R = red; X = spectral band of choice apart from B/G/R; PD = photodetector.

To overcome the limitations of conventional color sensing, a vertically stacked photodetector architecture would provide an attractive solution. This architecture involves the vertical stacking of photodetectors selectively responsive to different spectral regions and transparent elsewhere<sup>[2,5,8]</sup> (Figure 1b). Therefore, this approach would make color filters (and arrays thereof) unnecessary, thereby allowing color imaging without interpolation artifacts. Additionally, this approach would ultimately allow the entire pixel area to be used for light collection by all the photodetectors within a given pixel (Figure 1b), thereby enabling higher sensitivity and/or resolution (e.g., a fourfold improvement compared to conventional red-green-blue color-filtered architectures).<sup>[9]</sup> Ultimately, beyond red-green-blue color sensing/imaging, this approach could be seamlessly scaled—potentially without loss in photon collection

efficiency—to multispectral sensing/imaging by including additional photodetectors sensitive to adjacent spectral bands within the device stack (Figure 1c).

While color sensing based on vertically stacked photodetectors has been successfully demonstrated with silicon (reaching the market with the Foveon X3 image sensors),<sup>[10,11]</sup> the invariable, broadband absorption properties of silicon lead to spectral responsivities with comparatively large spectral widths,<sup>[12]</sup> affecting the complexity and noise performance of the resultant color detection scheme.<sup>[8]</sup> On the other hand, organic semiconductors have been identified as highly promising for vertically stacked color sensors due to their spectral tunability via facile chemical tailoring, which enables photodetectors inherently responsive to different spectral regions.<sup>[2,5,13]</sup> Beyond conventional color imaging applications, vertically stacked organic photodetectors can also be exploited for polarization-sensitive multicolor detection.<sup>[14,15]</sup> Moreover, organic photodetectors are also attractive due to their manufacturability via low-temperature solution-based methods (e.g., printing and coating) on flexible plastic substrates, which paves the way for the high-throughput and potentially low-cost fabrication of organic color sensors and imagers.<sup>[16–19]</sup> Importantly, compared to other emerging photodetector technologies also boasting spectral tunability and solution processability (e.g., lead halide perovskites and colloidal quantum dots),<sup>[7,20–24]</sup> organic semiconductors are carbon-based materials without toxic heavy metals in them, leading to a more benign sustainability profile.<sup>[25,26]</sup>

Despite considerable research efforts and industrial interest,<sup>[13,27–34]</sup> the monolithic integration of color sensors/imagers based on vertically stacked solution-processed organic photodetectors has remained a prominent, open challenge in the field. The significance of this challenge relates to the ambition of color-sensitive organic photodetector research as a whole: to seamlessly realize high-performance color sensors through the sequential deposition of inks of organic semiconductors and other printable functional layers.<sup>[18]</sup> An intermediate avenue reported in several studies to date involves a hybrid configuration, whereby an array of green-sensitive organic photodetectors is placed atop a pixelated silicon imager comprising a red-blue color-filter array<sup>[18,31–34]</sup> (Figure 1d). While delivering improved performance compared to conventional filter-based solutions, this approach generally suffers from similar limitations (e.g., half of the blue and red photons are dissipated in the color filters; see Figure 1d). In regard to reports pursuing filterless photodetector stacking, many of them rely on organic photodetectors processed on separate substrates and subsequently placed atop each.<sup>[9,13,14,35,36]</sup> Therefore, this

approach is inherently problematic from a manufacturing point of view: not only does it counter the promise of facile, high-throughput fabrication of color sensors and imagers, but it is also conducive to de-focusing, registration issues (which would eventually limit the yield or imager resolution achievable), and bulkiness.<sup>[36]</sup> Additionally, the remaining reports rely on vacuum-processed photoactive layers and spacers,<sup>[27–30,37]</sup> thereby blunting the technological edge of organic photodetectors over conventional technologies in terms of fabrication complexity and throughput.

The challenges associated with the solution-based, monolithic integration of a vertically stacked organic color sensor concern the optoelectronic properties of the photoactive layers, the device architecture, the electrical properties of the device stack, and processing constraints. At an *optoelectronic* level, it is necessary to deploy solution-processable organic photoactive layers that absorb light in different spectral regions and are concurrently capable of efficient photoconversion (Figure 1b), with matching electrodes that ensure efficient charge collection. At a *device architecture* level, solution-processable, transparent, insulating spacers are needed to electrically isolate adjacent photodetectors in the stack, enabling their independent biasing and current readout. Note that this aspect is essential to ensure the scalability of the vertically stacked architecture to multicolor sensing, marking a significant departure from the requirements of tandem and multi-junction solar cells.<sup>[38]</sup> Moreover, the front and intermediate electrodes of the photodetectors in the device stack need to have a high degree of transparency to allow photons to reach the target photoactive layer in the stack. At an *electrical* level, the bias voltages required to ensure adequate photoconversion in the various photodetectors in the stack should be minimized in order to prevent the breakdown of the photodetectors and their spacers. At a *processing* level, to ensure the physical integrity and functionality of the photodetectors in the stack, all layers should be orthogonal to the solvents used for the deposition of the layers immediately above, as well as resilient to the associated process steps; moreover, all layers should not require process temperatures that would damage the underlying layers in the stack. Such processing challenges are particularly critical and pose a significant constraint on the photoactive materials that can be adopted compared to the vast selection of functionally suitable organic semiconductors.<sup>[5]</sup> Based on all of challenges above, it is not surprising that the monolithic integration of a solution-based, vertically stacked organic color sensor has been elusive to date.

To advance the capabilities of solution-based organic photodetectors for color sensing, in this study we report, for the first time, the viability of a solution-based, modular platform for the monolithic integration of vertically stacked organic photodetectors for independent multi-color light sensing. As a proof-of-concept demonstration, we investigate the realization of a vertical device stack featuring two types of printable polymer-based photoactive layers capable of independently and concurrently sensing green and blue light. After illustrating the development and characterization of high-performance standalone photodetectors comprising these polymer-based photoactive layers, we present their monolithic integration in a vertical device stack. Specifically, we first discuss the strategies we devised to overcome the electrical, architectural, processing, and optoelectronic challenges underlying the realization of this device stack. Based on the resultant demonstration of the first monolithic, solution-based organic photodetector stack for independent, dual-color light sensing, and given the modularity of the approach pursued, we finally discuss the implications of our findings in terms of the future developments of high-performance organic color sensors and imagers.

## 2. Results and Discussion

Aiming to develop a platform for solution-processed, stacked, organic photodetectors toward high-performance multicolor light sensing, we reasoned that polymer-based photoactive layers would provide the ideal avenue. On the one hand, polymer semiconductors often lead to smoother and more uniform films compared to their small-molecule counterparts,<sup>[39–41]</sup> which is particularly desirable in multi-layer device stacks, given that morphological asperities are known to lead to shunts.<sup>[42,43]</sup> On the other hand, polymer semiconductors generally possess higher solvent resistance compared to their small-molecule counterparts,<sup>[44,45]</sup> thereby mitigating the constraints on the solvents that can be used when additional layers are solution-deposited onto the device stack.

To realize a proof-of-concept demonstration of solution-processed stacked photodetectors independently selective to green and blue light, we considered stacking a green-sensitive photodetector atop a blue-sensitive photodetector. While polymer-based photoactive layers would provide the ideal avenue for solution-based photodetector stacking, the broadband absorption character of conjugated polymers generally prevents the realization of narrowband-absorption-type polymer-based photodetectors (i.e., color-selective photodetectors that absorb light only within the target spectral range).<sup>[5,46]</sup> However, we reasoned that, due to stacking, a green selective photodetector could be simply obtained from a broadband photoactive layer

with an absorption onset at the long-wavelength edge of the green range. By placing such a photodetector atop a narrowband-absorption-type blue-selective photodetector, blue photons would be dissipated in the latter, thereby allowing only longer-wavelength photons (e.g., green and red photons) to reach deeper into the photodetector stack. In such a case, the broadband polymer-based photoactive layer with absorption onset at the long-wavelength edge of the green range would effectively behave as a green-selective light sensor.

Based on the aforementioned aims and constraints, we considered investigating poly(9,9-dioctylfluorene-alt-bithiophene) (F8T2) as the blue-absorbing polymeric component of the photoactive layer for blue-selective photodetection and poly[2-methoxy-5-(2'-ethylhexyloxy)-1,4-phenylene vinylene] (MEH-PPV) for green-responsive photodetection, as detailed in the following. The molecular structures of the two materials are displayed in **Figure 2a**. In addition to their suitable optoelectronic properties and device performance (see below), these polymers were selected due to their facile synthesis,<sup>[47-49]</sup> wide commercial availability, and low cost amongst organic semiconductors. Indeed, ease of synthesis has been identified as essential for the industrial scale-up of organic semiconductor technologies.<sup>[50,51]</sup>

### **2.1. Characterization of F8T2- and MEH-PPV-Based Films**

The choice of F8T2 for blue-selective light detection was based on its thin-film optical gap of 2.42 eV (see the Tauc plot in Figure 2b) and corresponding absorption onset wavelength of  $\lambda_{\text{abs,on}} = 512$  nm, which is ideal for blue-selective narrowband-absorption-type photodetectors. The HOMO and LUMO levels of F8T2 thin films were at 5.27 eV and 2.85 eV, respectively, below the vacuum level, as determined via ultraviolet photoelectron spectroscopy (UPS) and ultraviolet-visible (UV-Vis) spectrophotometry (see Figure 2b-c). Therefore, we resolved to blend F8T2 with phenyl-C<sub>61</sub>-butyric acid methyl ester (PCBM; see Figure 2a) to realize bulk heterojunctions that could enable efficient blue-selective narrowband-absorption-type photodetectors. Indeed, while the latter manifests an absorption tail through the visible range, its absorption coefficient in the green and red spectral regions is more than fifteen times smaller than the absorption coefficient of F8T2 in the blue spectral region, allowing balanced F8T2:PCBM blends (i.e., 1:1 by weight) to be also highly absorbing in the blue spectral region (Figure 2d). The measured photoluminescence spectra of F8T2, PCBM, and F8T2:PCBM (1:1) films confirmed adequate quenching of the luminescence in F8T2:PCBM films (Figure 2e), consistent with the literature.<sup>[52]</sup> Furthermore, F8T2:PCBM (1:1) blends delivered compact, ultra-smooth films with a root-mean-square (RMS) roughness of only 0.5 nm (Figure 2f), which

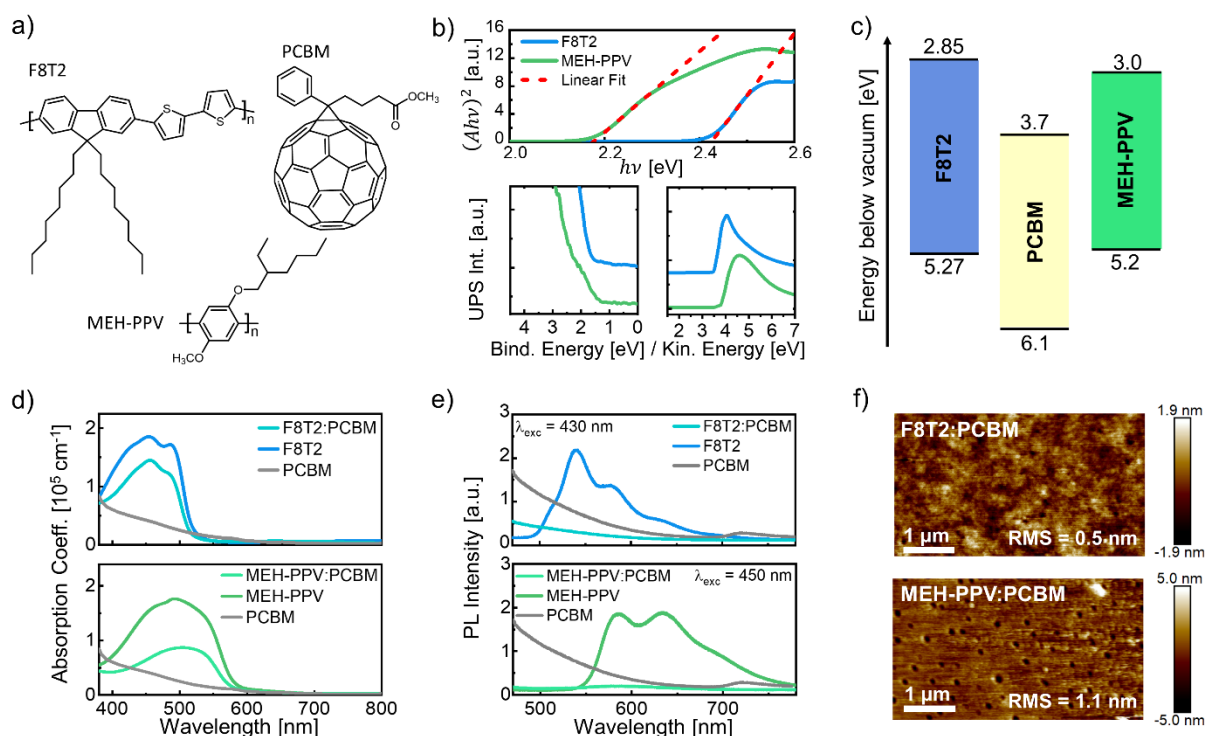


**Figure 2.** a) Molecular structures of the materials used in the study. b) (top) Plots of  $(Ah\nu)^2$  versus the photon energy  $h\nu$  (i.e., Tauc plots) for F8T2 and MEH-PPV films, where  $A$  is their measured absorbance; (bottom) UPS intensity (valence band states (left) and He I secondary electron onset (right)) from F8T2 and MEH-PPV films. c) Energy levels of the different materials used in this study. d) Absorption coefficients of PCBM,<sup>[53]</sup> F8T2, F8T2:PCBM (1:1), MEH-PPV, MEH-PPV:PCBM (1:1). e) Corresponding photoluminescence (PL) spectra. f) Atomic force microscopy images of F8T2:PCBM (1:1) and MEH-PPV:PCBM (1:1) films.

denotes good mixing between the two materials, as also highly desirable for the integration of such films in a multi-layer device stack.

We investigated MEH-PPV for the realization of green-responsive photodetectors firstly due to its strong absorption of green photons (Figure 2d), thanks to its optical gap of 2.17 eV (see Tauc plot in Figure 2b), which is approximately at the low-energy edge of the green spectral region. The experimentally determined HOMO and LUMO levels of spin-coated MEH-PPV films were at 5.2 and 3.0 eV, respectively, below the vacuum level (see Figure 2b-c). Measured photoluminescence spectra of MEH-PPV, PCBM, and MEH-PPV:PCBM (1:1) films (see Figure 2e) confirmed the quenching of the photoluminescence of MEH-PPV once it was blended with PCBM in a 1:1 ratio (by weight), consistent with the literature.<sup>[54]</sup> Additionally,

given the much larger absorption coefficient of MEH-PPV compared to PCBM (Figure 2d), MEH-PPV:PCBM (1:1) films manifested comparatively little absorbance beyond the onset wavelength of MEH-PPV (Figure 2d), which is ideal for green-sensitive photodetection. Finally, the spin-coated MEH-PPV:PCBM films had an RMS roughness of only 1.1 nm (Figure 2f), making them appealing for incorporation in a multilayer device stack.

## 2.2. F8T2-Based Blue-Sensitive Photodetectors

We first pursued the realization of standalone F8T2-based and MEH-PPV-based photodetectors to assess their ultimate photodetection capabilities for blue- and green-responsive photodetection, respectively, free of the processing constraints of the stacked device architecture. Specifically, we fabricated F8T2-based photodetectors by sandwiching a 160-nm-thick F8T2:PCBM film between a PEDOT:PSS | indium-tin oxide (ITO) anode and an aluminum cathode (**Figure 3a**).

The external quantum efficiency (EQE) spectra are shown in Figure 3b. Such spectra reveal a blue-selective response in agreement with the absorbance of the F8T2 and F8T2:PCBM films. A steep edge was observed at  $\lambda \cong 520$  nm (Figure 3b), which closely follows the absorption onset of F8T2 (see above). The EQE peaked at  $\lambda_{p,EQE} \cong 454$  nm, precisely matching the absolute maximum of the absorbance of F8T2 and F8T2:PCBM films. In particular, in self-powered operation ( $V_{BIAS} = V_{Al} - V_{ITO} = 0$  V), the peak external quantum efficiency,  $EQE_p = EQE(\lambda_{p,EQE})$  amounted to 20.7 %, denoting efficient photoconversion in the blue spectral region. Further,  $EQE_p$  increased with  $V_{BIAS}$ , reaching 45.8 % at  $V_{BIAS} = 3$  V (Figure 3b), making these photodetectors highly efficient for blue-selective light detection. The corresponding responsivity  $R$  ( $R = J_{ph} / P_{in}$ , where  $J_{ph}$  is the photocurrent density and  $P_{in}$  is the optical power density) followed the same trend, reaching up to 174 mA W<sup>-1</sup> in the blue spectral region at  $V_{BIAS} = 3$  V (Figure 3c); concurrently, the specific detectivity in the shot noise limit,  $D_{sn}^*$ , (i.e.,  $D_{sn}^* = R / (2 q J_d)^{1/2}$ , where  $J_d$  is the measured dark current density; see Figure S1) reached a maximum of  $3.3 \cdot 10^{12}$  Jones (Figure 3c), which is in line with the general organic photodetector literature.<sup>[5]</sup> The increases in EQE and responsivity with  $V_{BIAS}$  can be traced to the higher efficiency achieved in terms of exciton dissociation and/or carrier collection as the applied voltage rises.<sup>[55]</sup> Importantly, such EQE values are among the highest for blue-selective narrowband-absorption-type organic photodetectors.<sup>[7]</sup>

In addition to a strong photoresponse in the blue range, F8T2:PCBM photodetectors also provided robust rejection of photons outside the target spectral range (Figure 3b). The residual response in the green spectral region can be traced to the absorption properties of PCBM (see Figure 2d), whose domains therefore also contributed to the photocurrent. However, given the superior absorption properties of F8T2, the out-of-band photocurrent response was minor and did not compromise the spectrally selective character of the F8T2:PCBM photodetectors. For instance, the F8T2:PCBM photodetectors delivered an EQE spectral rejection ratio<sup>[5]</sup>  $SRR_{EQE}(\lambda_{p,EQE}, 570 \text{ nm}) = EQE(\lambda_{p,EQE})/EQE(570 \text{ nm})$  of  $\sim 13$  and independent of the bias voltage with respect to the wavelength  $\lambda_{green} = 570 \text{ nm}$ , which represents the onset of the green spectral range.

The F8T2:PCBM photodetectors exhibited a linear photoresponse, as determined from their photocurrent-optical power characteristics (Figure 3d). Such characteristics were measured using an LED source narrowly emitting around  $\lambda = 455 \text{ nm}$ , consistent with the intended real-world use of such photodetectors for blue-light sensing. The least-square fit of the measured photocurrent data as a function of the optical power conforms to the relationship

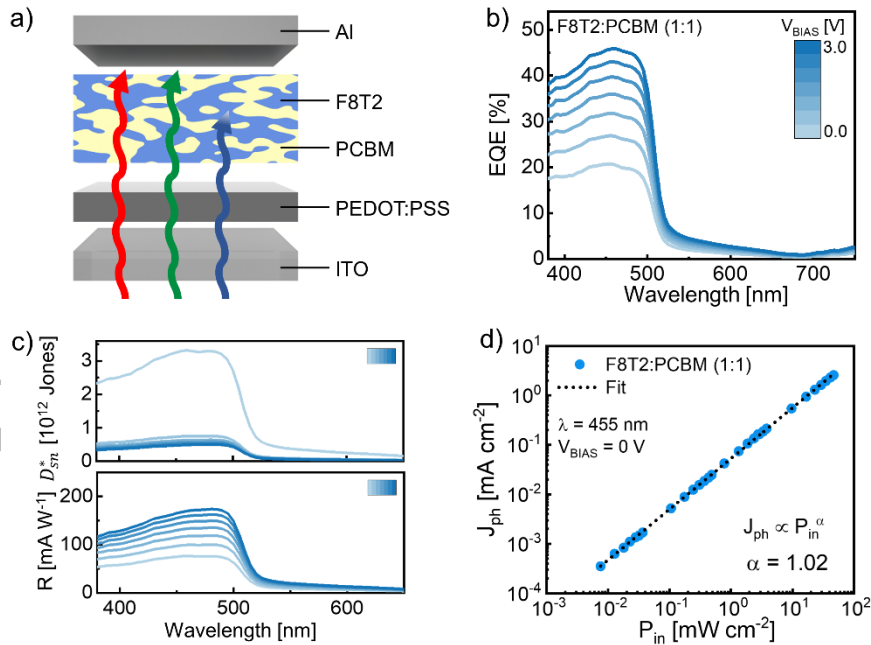


**Figure 3.** F8T2-based blue-sensitive photodetectors: a) device structure; b) EQE spectra at different reverse bias voltages; c) spectral responsivity (bottom) and specific detectivity in the shot noise limit (top); d) photocurrent density  $J_{ph}$  versus optical power density  $P_{in}$  at  $\lambda = 455 \text{ nm}$  and  $V_{BIAS} = 0 \text{ V}$ . A fit of the type  $J_{ph} \propto P_{in}^{\alpha}$  is overlaid on the measured dataset.

$J_{ph} \propto P_{in}^{\alpha}$  with  $\alpha = 1.02$ , i.e., which is essentially indistinguishable from unity given the uncertainty limits associated with the measurement and the fitting routine. This result indicates that the F8T2:PCBM layers were not burdened with trap states intersecting the quasi-Fermi levels in the photoactive material as the incident optical power was raised.<sup>[56–58]</sup> Additionally, this result confirms the suitability of these photodetectors for real-world applications, which generally require not only color-discrimination capabilities but also the quantitative determination of the incident optical power, for which a linear photoresponse is essential.<sup>[59,60]</sup> In fact, the observed linear behavior spanned more than four orders of magnitude, given that the optical power range probed was not limited by the device response but by characterization equipment used. Therefore, these photodetectors possessed a linear dynamic range greater than 76 dB, if we estimate the lower limit of the linear dynamic range as  $LDR_U = 20 \log(J_{ph,max}^{(meas)}/J_{ph,min}^{(meas)})$ , where  $J_{ph,max}^{(meas)}$  and  $J_{ph,min}^{(meas)}$  are the upper and lower bounds of the photocurrent in the linear region that could be probed with our experimental apparatus.

### 2.3. MEH-PPV-Based Green-Sensitive Photodetectors

In line with the goal of realizing vertically stacked multicolor light sensors, we additionally investigated MEH-PPV-based green-sensitive photodetectors. We first realized MEH-PPV:PCBM devices with the same architecture as the F8T2-based counterparts, comprising a spin-coated 360-nm-thick active layer (**Figure 4a**). However, we found that devices comprising 1:1 (by weight) MEH-PPV:PCBM films did not deliver a strong photoresponse (**Figure 4b**). Therefore, we investigated photodetectors with active layers having different MEH-PPV:PCBM blending ratios: 1:4, 1:2, 1:1, 2:1 (by weight). By comparing the EQE spectra of the corresponding photodetectors, we found that those with a 1:4 blend gave the strongest photoresponse (**Figure 4b**). Correspondingly, we measured higher photoluminescence quenching from MEH-PPV:PCBM films with such a blending ratio (**Figure 4c**). Therefore, the enhanced photoresponse from the 1:4 MEH-PPV:PCBM devices can be rationalized in terms of the higher photogeneration efficiency (via enhanced exciton dissociation) enabled by the 1:4 MEH-PPV:PCBM films. Based on this result, we adopted a 1:4 ratio for the MEH-PPV:PCBM photoactive layers in the rest of our study.

The EQE spectra of the MEH-PPV-based photodetectors closely followed the absorption spectrum of MEH-PPV thin films, with a steep rise at around 570 nm and a strong photoresponse at 450–550 nm (**Figure 4d**). The peak EQE amounted to  $EQE_p = 31.2\%$  in self-powered operation. Additionally,  $EQE_p$  reached 56.9% as the reverse bias voltage was

increased to 3 V (Figure 4d), consistent with the enhancement of the exciton dissociation efficiency and/or carrier collection efficiency.<sup>[55]</sup> Among green-sensitive solution-processed organic photodetectors operating in primary photocurrent mode reported to date, this represents one of the highest efficiencies<sup>[16,55]</sup> and marks a more than 50 % increase compared to prior work on MEH-PPV:PCBM photodetectors.<sup>[61]</sup> This performance increase can be traced to our optimization of the photoactive layer composition. Concurrently, as shown in Figure 4e, the spectral responsivity peaked at  $230 \text{ mA W}^{-1}$  in the green spectral region, while the maximum specific detectivity in the shot noise limit,  $D_{sn}^*$ , amounted to  $4.8 \cdot 10^{12}$  Jones, which is comparable to the performance of the F8T2-based photodetectors reported above.

A shallow photoresponse tail was observed from MEH-PPV:PCBM devices beyond the absorption onset of MEH-PPV (Figure 4d), which can be traced to the photogeneration ensuing photon absorption in the PCBM domains. To quantitatively assess the ability of

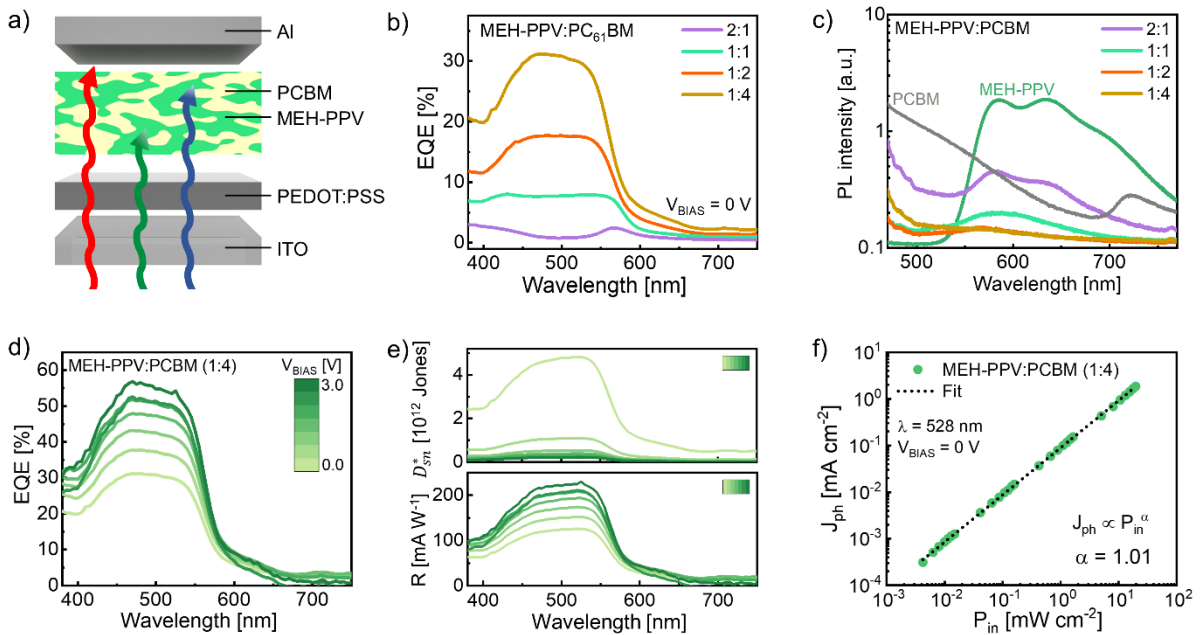


**Figure 4.** MEH-PPV-based green-sensitive photodetectors: a) device structure; b) EQE spectra of photodetectors featuring MEH-PPV:PCBM layers with different blending ratios ( $V_{BIAS} = 0$  V); c) PL spectra of MEH-PPV:PCBM layers with different blending ratios; d) EQE spectra of MEH-PPV:PCBM (1:4) photodetectors at different reverse bias voltages; e) spectral responsivity (bottom) and specific detectivity in the shot noise limit (top) of MEH-PPV:PCBM (1:4) photodetectors; f) photocurrent density  $J_{ph}$  versus optical power density  $P_{in}$  at  $\lambda = 528$  nm and  $V_{BIAS} = 0$  V. A fit of the type  $J_{ph} \propto P_{in}^\alpha$  is overlaid on the measured dataset.

MEH-PPV:PCBM to selectively detect green photons over red photons, we quantified the EQE spectral rejection ratio  $SRR_{EQE}(500 \text{ nm}, \lambda_{\text{red}}) = EQE(500 \text{ nm})/EQE(\lambda_{\text{red}})$ , given that  $\lambda = 500 \text{ nm}$  is within the photoresponse plateau in the green spectral region and  $\lambda_{\text{red}} = 650 \text{ nm}$  is representative of the red spectral range. We found that  $SRR_{EQE}$  was greater than  $\cong 10$  at low applied bias and went up to 32 at -2.5 V. Therefore, in addition to enabling efficient green-responsive light detection, MEH-PPV:PCBM photodetectors adequately rejected photons in the red spectral range, as desired for color-sensing applications.

The photocurrent-optical power characteristics of the MEH-PPV:PCBM photodetectors confirmed their robust linearity (Figure 4f). We studied their photocurrent-optical power dependence using a green LED source narrowly emitting around  $\lambda = 528 \text{ nm}$ , in line with their intended application for green-light sensing. The measured photocurrent data followed a trend of the type  $J_{ph} \propto P_{in}^{\alpha}$  with  $\alpha = 1.01$  throughout the optical power range that could be probed with our apparatus, spanning four orders of magnitude. The corresponding lower limit of the linear dynamic range,  $LDR_U = 20 \log(J_{ph,max}^{(meas)}/J_{ph,min}^{(meas)})$ , amounted to 74 dB. We emphasize that this represents a lower limit on the linear dynamic range of the MEH-PPV:PCBM photodetectors, given that the span of the probed range was limited by the light source and acquisition electronics used.

#### 2.4. Solution-Based Integration of Vertically Stacked Photodetectors for Color Sensing

To assess the viability of integrating solution-based organic photodetectors toward multi-color light sensing, we considered realizing a stacked device structure with blue-selective F8T2-based devices at the bottom and green-responsive MEH-PPV-based ones at the top (Figure 5a). We additionally aimed to engineer a modular device architecture that could be adapted in the future to the stacking of several photodetectors to cover more spectral bands (e.g., for multispectral imaging). Therefore, instead of fabricating the MEH-PPV-based devices directly atop the F8T2-based ones (which could not be scaled up to vertically stacked pixels with photodetector count  $> 2$ ), we pursued the adoption of an insulating spacer between the two types of photodetectors as a means of allowing their independent voltage biasing and photocurrent readout. Specifically, we considered solution-processed poly(methyl methacrylate) (PMMA) to realize such a spacer (Figure 5a). Alongside the low cost and wide availability of PMMA, this choice was motivated by the excellent insulating and film-forming properties of PMMA, as confirmed by its use as gate dielectric in high-performance thin-film transistors.<sup>[62,63]</sup> Moreover, PMMA could potentially address the processing challenge associated with the realization of a

multi-level vertically stacked photodetector architecture (Section 1). Indeed, PMMA can be generally processed from solvents that are orthogonal to a wide range of polymer semiconductors<sup>[64,65]</sup> and its high-molecular-weight embodiments have good resistance to organic solvents commonly used for the solution-based processing of organic semiconductors.

As we assessed the viability of using a PMMA layer as a spacer (see the device architecture in Figure 5a), we found that, if we adopted the same deposition procedures for the different solution-processed layers that we had optimized for standalone photodetectors, we could not obtain working MEH-PPV-based photodetectors in the stacked device configuration. Specifically, by visual inspection, we found that cracks were formed in the MEH-PPV:PCBM layer, which eventually prevented us from acquiring meaningful photodetector data from such devices. However, we found that we could overcome this issue if we subjected the samples to oxygen plasma before and after spin-coating the PMMA spacer (see Figure 5a for the overall device architecture), thus obtaining functional devices (see discussion below). Given that oxygen plasma treatments are known to enhance the hydrophilicity of polymer layers,<sup>[66]</sup> this finding points to the important role of interfacial properties for the solution-based monolithic stacking of photodetectors based on organic layers.

In light of the *device architecture* challenge associated with photodetector stacking (Section 1), an additional design choice we faced concerns the electrode materials. In a stacked photodetector architecture, all photodetector electrodes except the topmost one should have large transmittance within the target spectral regions of the overlying photodetectors. To this end, we considered adopting ultrathin, semitransparent metal electrodes for the cathode of the F8T2-based photodetectors and anode of the MEH-PPV-based photodetectors (Figure 5a). This choice was prompted by the facile deposition of metal thin films within an academic laboratory, consistent with the aim of our study to provide a proof-of-principle demonstration of monolithically stacked solution-based organic photodetectors. Nonetheless, we envisage that solution-processed semi-transparent electrodes—which are being intensively investigated by the printable optoelectronics community<sup>[67–69]</sup>—will provide a valuable opportunity for the future scaling up of our approach.

To realize ultrathin, semi-transparent cathodes for the F8T2:PCBM devices in the photodetector stack, we adopted a configuration based on an Al | Au bilayer. We conjectured that an ultrathin aluminum layer atop the F8T2:PCBM film would preserve the efficient electron extraction

achieved with the thick aluminum cathode employed in the standalone F8T2:PCBM devices (Section 2.2). Further, we considered capping the ultrathin Al layer with an ultrathin Au layer as a means of mitigating the oxidation of the former<sup>[70,71]</sup> while enhancing the conductivity of the overall cathode. We tested the viability and effectiveness of this approach on reference devices. We firstly varied the thickness of the aluminum layer for a fixed 20-nm-thick Au capping layer, finding that a 5-nm-thick Al layer was sufficient to deliver optimum EQE (Figure S2). Subsequently, we set the thickness of the Al layer and investigated the impact of different thicknesses of the Au layer atop. While 3-nm-thick Au atop 5-nm-thick Al delivered reference devices with particularly low EQE (Figure S2), it was found that an Al (5 nm) | Au (5 nm) cathode gave F8T2:PCBM devices with comparable EQE as the standalone devices with at 80-nm-thick Al cathode (see below). Moreover, we assessed the transmittance of the Al (5 nm) | Au (5 nm) bilayer, given its impact on the overall functionality of the stacked device architecture. We found that the Al (5 nm) | Au (5 nm) bilayer on glass had a transmittance of

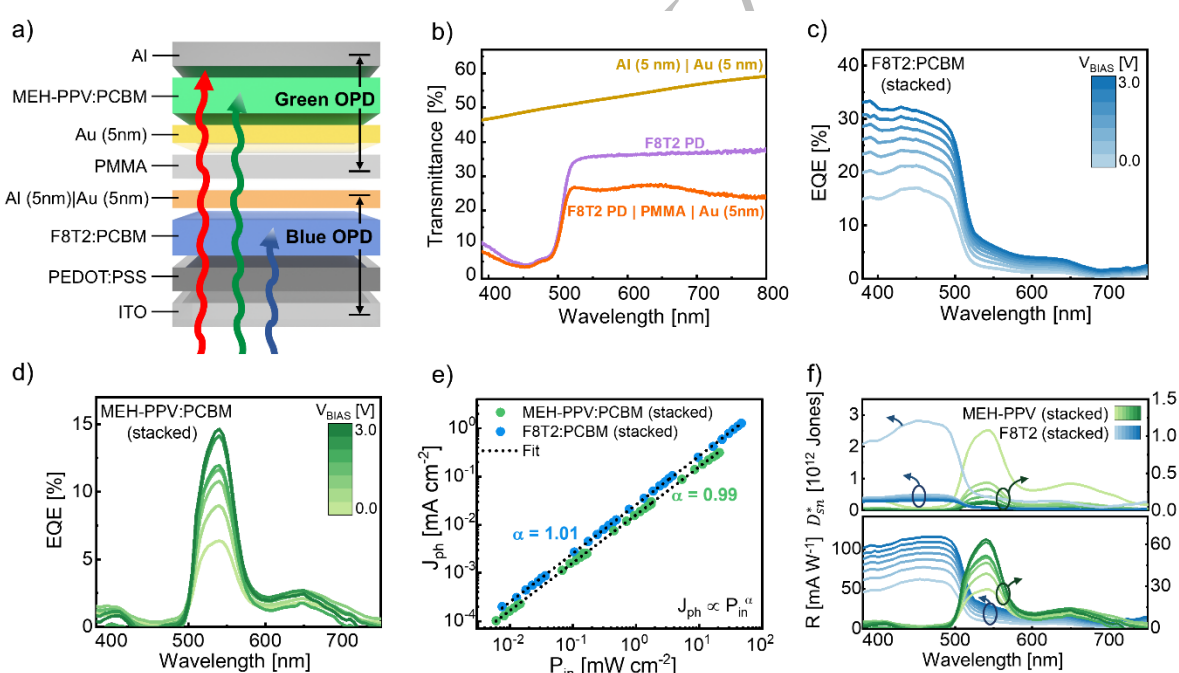


**Figure 5.** a) Solution-based, monolithic integration of vertically stacked organic photodetectors. b) Transmittance through different portions of the device stack. c) Stacked F8T2-based photodetector and d) stacked MEH-PPV-based photodetector: EQE spectra at different bias voltages. e) Photocurrent-optical power characteristics of stacked F8T2-based and MEH-PPV-based photodetectors. f) Responsivity (bottom) and specific detectivity in the shot noise limit (top) of stacked F8T2-based and MEH-PPV-based photodetectors at different bias voltages between 0 and 3 V in steps of 0.5 V (darker colors correspond to higher bias voltage values).

more than 50% in the green and red spectral regions (see the trace labeled ‘Al (5 nm) | Au (5 nm)’ in Figure 5b), thereby being compatible with a vertically stacked device architecture. Furthermore, we assessed the optical effect of the Al (5 nm) | Au (5 nm) electrode by determining the transmittance of the ITO | PEDOT:PSS | F8T2:PCBM | Al (5 nm) | Au (5 nm) stack, thereby mimicking the stack that incident light would traverse before reaching the upper photodetector in the overall device stack depicted in Figure 5a. We found that such transmittance in the green and red spectral regions amounted to 36–37 % (see the trace labeled ‘F8T2 PD’ in Figure 5b), revealing the additional aggregate effect of the transmittance of the ITO | PEDOT:PSS | F8T2:PCBM stack.

To ensure that green photons transmitted by the F8T2:PCBM photodetectors could be harvested by the overlying MEH-PPV-based photodetectors, it was also necessary to develop a semitransparent anode for the latter. Therefore, we investigated the possibility of using ultrathin Au layers for this purpose—in lieu of the ITO anodes used in standalone MEH-PPV-based photodetectors (see Section 2.3), whose deposition via conventional sputtering methods would damage the underlying organic layers.<sup>[72,73]</sup> We found that working MEH-PPV-based photodetectors could be fabricated with Au anodes as thin as 5 nm. To assess the optical impact of such ultrathin anodes in the target device stack (Figure 5a), we measured the transmittance of the ITO | PEDOT:PSS | F8T2:PCBM | Al (5 nm) | Au (5 nm) | PMMA | Au (5 nm) stack, which mimics the stack that incident light needs to traverse before reaching the MEH-PPV-based photoactive layer atop. We found that the resultant transmittance amounted to 26–27 % in the green and red spectral regions (see the trace labeled ‘F8T2 PD | PMMA | Au (5 nm)’ in Figure 5b), signifying that an appreciable fraction of the incident photons could reach the upper photodetector in the overall device stack shown in Figure 5a. Therefore, we concluded that the adopted solution would enable us to assess the viability of monolithically integrating organic photodetectors based on solution-processed photoactive layers alongside a solution-processed spacer. Nonetheless, we foresee that electrodes with greater transmittance<sup>[68,69]</sup> could be adopted in the future, which therefore constitutes a worthwhile goal for follow-up studies.

Building on the findings above, we first realized and characterized the photodetector stack shown in Figure 5a, comprising MEH-PPV-based devices atop F8T2-based devices, with a PMMA spacer in between and ultrathin, semi-transparent electrodes. The resultant EQE spectra of the F8T2:PCBM devices within the stack are shown in Figure 5c. These spectra reveal that the EQE follows similar trends both in wavelength and voltage as the standalone F8T2:PCBM

devices discussed earlier, giving a strong photoresponse in the blue spectral region and robust rejection of lower-energy (e.g., red and green) photons. However, closer inspection of the EQE spectra reveals that the peak EQE is slightly lower than that of standalone devices, but nonetheless up to 33.3 % at  $V_{\text{BIAS}} = 3.0$  V. We found that this reduction can be traced to the oxygen plasma treatment needed to achieve stacked monolithic integration (see Figure S3), likely due to the oxidative impact of the residual oxygen plasma species penetrating the photoactive layer during this processing step.<sup>[74,75]</sup>

After integration within the stacked architecture, the solution-based MEH-PPV:PCBM devices exhibited pronounced spectral selectivity toward green photons, confirming the merits of this architecture for multicolor light sensing. This finding reflects the dissipation of blue photons in the underlying F8T2:PCBM layer, which allows only green and red photons to reach the upper photodetector. Specifically, the stacked MEH-PPV:PCBM devices deliver a peak EQE up to  $\text{EQE}_p = 14.6\%$  at  $\lambda_{p,\text{EQE}} = 540$  nm for  $V_{\text{BIAS}} = 3$  V, with the corresponding full width at half maximum amounting to  $\text{FWHM}_{\text{EQE}} = 53$  nm. Further, the stacked photodetectors exhibited good spectral rejection of both blue and red light, with  $\text{SRR}_{\text{EQE}}(\lambda_{p,\text{EQE}}, 400 \text{ nm}) = 19$  and  $\text{SRR}_{\text{EQE}}(\lambda_{p,\text{EQE}}, 650 \text{ nm}) = 6$ , respectively. Such performance parameters reveal the robustness of the stacked MEH-PPV:PCBM devices for green-selective light sensing.

It is worth noting that the EQE spectra of the stacked MEH-PPV:PCBM devices closely followed the EQE of the standalone MEH-PPV:PCBM devices, once the transmission losses of the various layers in the stack are taken into account (Figure S4). Indeed, by multiplying the EQE of a standalone MEH-PPV:PCBM photodetector with the experimentally measured transmittance of the underlying stack (i.e., ITO | PEDOT:PSS | F8T2:PCBM | Al (5 nm) | Au (5 nm) | PMMA | Au (5 nm); see the trace labeled F8T2 PD | PMMA | Au (5nm) in Figure 5b), we obtained an expected peak EQE value of 14.5% (Figure S4), which is in remarkable agreement with the one experimentally measured from the stacked device (i.e., 14.6%). This implies that, for future improvements of the photoconversion efficiency of such stacked MEH-PPV:PCBM photodetectors, a straightforward strategy would involve the adoption of electrodes with higher transmittance, which therefore encourages future efforts in this direction.

The stacked F8T2:PCBM and MEH-PPV:PCBM devices delivered a linear photoresponse (Figure 5e). Their responsivities and specific detectivities (Figure 5f) were also comparable to

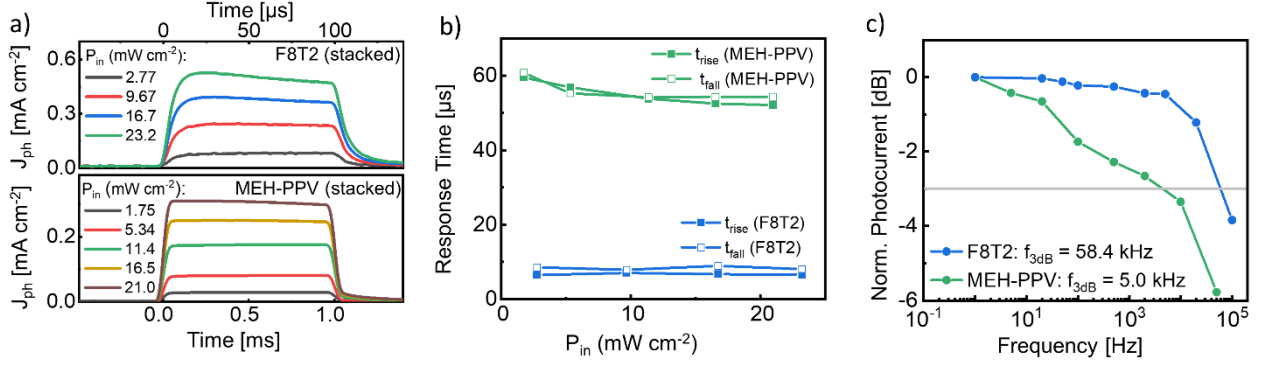


**Figure 6.** a) Photocurrent response of a stacked F8T2-based photodetector (top) and a stacked MEH-PPV-based photodetector (bottom) at different values of the incident optical power (see the legend). Corresponding b) rise and fall times and c) frequency response.

the standalone counterparts (Figure 3d, 4f), apart from the narrowband character acquired by the MEH-PPV:PCBM devices and the EQE reduction due to the electrodes adopted.

Finally, we characterized the speed of response of our stacked color-sensitive photodetectors, both in the time and frequency domains. Figure 6a shows the photocurrent response to rectangular light pulses of different optical power, while the corresponding rise and fall times are displayed in Figure 6b. Both types of stacked photodetectors have response times well below 100 μs. Specifically, F8T2-based and MEH-PPV-based devices have response times of 8 μs and 55 μs, respectively, essentially insensitive to the incident optical power. The faster response of the F8T2-based devices matches their behavior in the frequency domain, where they deliver a 3dB frequency of 58 kHz. By contrast, the MEH-PPV-based devices give a 3dB frequency of 5 kHz. Overall, the response of both types of stacked photodetectors is much faster than typically required for color imaging,<sup>[5]</sup> confirming their potential for real-world applications.

### 3. Conclusions

Our study has demonstrated, for the first time, the solution-based monolithic integration of vertically stacked organic photodetectors, which has long been sought after to realize high-performance, inexpensive color sensors beyond the limitations of conventional, filter-based technologies. Given the optoelectronic and processing constraints of this architecture, we first developed polymer-based photodetectors featuring F8T2:PCBM and MEH-PPV:PCBM active layers, which we optimized to achieve high photoconversion efficiency and a linear photoresponse in the blue and green spectral regions, respectively. To realize a modular,

monolithic device architecture of vertically stacked photodetectors, we additionally developed a solution-deposited insulating spacer made of PMMA to allow the independent biasing and readout of the stacked photodetectors, and semi-transparent electrodes to allow light to penetrate the device stack. By integrating all of these elements, we realized the first solution-based device stack featuring two vertically stacked organic photodetectors selectively responding to blue and green light. Such stacked photodetectors featured responsivities in the region of 60–100 mA W<sup>-1</sup> in both spectral ranges, linear dynamic ranges greater than four orders of magnitude, large spectral rejection ratios with respect to adjacent spectral regions, and response times shorter than 60 μs—hence, meeting the operational requirements for real-world applications. Given the modularity of our architecture and through the future deployment of printable semitransparent electrodes, our work illustrates the formidable opportunity provided by organic semiconductors to go beyond the limitations of conventional, silicon-based approaches to color sensing, paving the way for low-cost color imagers seamlessly covering multiple spectral regions with high sensitivity and resolution.

#### 4. Experimental Section

*Materials:* The following chemicals were purchased and used without further purification: F8T2 (mass-average molar mass  $M_w > 20\,000$ ; Lumtec), MEH-PPV ( $M_w > 10\,000$ ; Lumtec), PCBM (> 99.5%, Lumtec), PMMA ( $M_w > 120,000$ ; Sigma-Aldrich), chlorobenzene (99.8%, anhydrous; J&K), 1,2-dichlorobenzene (99%; Sigma-Aldrich), n-butyl acetate (99%, superdry; J&K), PEDOT:PSS (Clevios P VP Al 4083; Heraeus), acetone ( $\geq 99.5\%$ , AR; YongHua), ethanol (AR; YongHua), aluminum (99.999%; Zhongnuoxincai, Beijing Technology Co., Ltd), gold (99.999%; Zhongnuoxincai, Beijing Technology Co., Ltd). ITO-coated glass substrates were purchased from South China Science & Technology Co., Ltd. Glass substrates were purchased from Guangzhou Lighting Glass Co., Ltd.

*Solution Preparation:* Solutions of F8T2, PCBM and their blends were prepared by dissolution of their powders in 1,2-dichlorobenzene within a nitrogen-filled glove box. In regard to blends used for device fabrication, each compound was dissolved at a concentration of 40 g L<sup>-1</sup>. The solutions were stirred at 40 °C for more than 4 hours before mixing. Subsequently, the F8T2 and PCBM solutions were mixed in a 1:1 ratio (by weight) and stirred overnight. Solutions of MEH-PPV, PCBM and their mixtures were prepared in the same environment. MEH-PPV was dissolved in chlorobenzene at a concentration of 10 g L<sup>-1</sup> and PCBM at a concentration of 40 g L<sup>-1</sup>. Then, MEH-PPV and PCBM solutions were mixed in the following ratios: 2:1, 1:1, 1:2

and 1:4 (by weight). The resultant solutions were then stirred overnight. PMMA powder was dissolved in n-butyl acetate at a concentration of 80 g L<sup>-1</sup> and stirred for 48 hours.

*Photodetector Fabrication:* ITO-coated glass substrates were cleaned in an ultrasonic bath, first in acetone, then in ethanol, and finally in deionized water (15 min for each step). Subsequently, the substrates were dried in ultrapure nitrogen gas and were exposed to an oxygen plasma for 10 min (Harrick, PDC-002). After being filtered (PTFE filter, 0.45 μm pore size), the PEDOT:PSS suspension was spin coated (at 5000 rpm for 40 s) on the substrates. The samples were then annealed on a hot plate at 100 °C for 15 min in air ambient condition.

In regard to standalone F8T2:PCBM photodetectors, the mixed solution of F8T2 and PCBM (1:1) was spin-coated (1000 rpm for 40 s) onto the samples to obtain 160-nm-thick films, which were then annealed at 80 °C for 10 min. In regard to standalone MEH-PPV:PCBM photodetectors, the mixed solutions of MEH-PPV and PCBM were spin coated (1000 rpm for 40 s) onto the samples. Subsequently, the samples were then annealed at 90 °C for 10 min, resulting in MEH-PPV:PCBM films with a thickness of 360 nm. After the deposition of the active layer, an 80-nm-thick Al cathode was thermally evaporated onto the samples at a pressure below 2·10<sup>-6</sup> mbar through a shadow mask.

In regard to the stacked photodetectors, after the F8T2:PCBM film was deposited, 5 nm Al and 5 nm Au layers were thermally evaporated sequentially through shadow masks. After an oxygen plasma cycle (10 min), a 560-nm-thick PMMA film was spin-coated (2000 rpm for 40 s), followed by an additional oxygen plasma cycle (10 min). Subsequently, a 5-nm-thick Au anode was evaporated through a shadow mask. After the deposition of a 220-nm-thick MEH-PPV:PCBM layer by spin coating, an 80-nm-thick Al layer was thermally evaporated onto the samples.

*Characterization:* UV-vis absorption spectra of organic semiconductor films on quartz were measured with a LAMBDA 750 spectrophotometer (PerkinElmer). Steady-state photoluminescence spectra were measured with an FL3 fluorometer (HORIBA Scientific). The thickness of the organic films was measured with a step profiler (KLA-Tencor-D100). The roughness of the organic semiconductor films was measured using a Veeco Multimode V atomic force microscope (Bruker) in tapping mode. Ultraviolet photoelectron spectroscopy was conducted using a ThermoFisher ESCALAB Xi+ system. Dark current-voltage characteristics

were measured in air with a Keithley 6420 source meter. EQE spectra were measured with a custom-made setup comprising an Omni- $\lambda$ 2005i monochromator (Zolix), a power meter (Thorlabs, PM200), and a calibrated silicon sensor (Thorlabs, S120VC). Transient photocurrent and frequency measurements were conducted with a custom-made setup relying on 455 nm and 528 nm LEDs controlled with a USB-6001 data acquisition device (National Instruments) and the current signal amplified by a DHPCA-100 amplifier (FEMTO).

### **Supporting Information**

Supporting Information is available from the Wiley Online Library or from the author.

### **Acknowledgements**

T. Z. and V. P. contributed equally to this work. V. P. acknowledges financial support from the National Natural Science Foundation of China (61805166).

### **Author Contributions**

T. Z. carried out the bulk of the fabrication and characterization experiments and data analysis. K. X. designed the masks for the vertically stacked devices and contributed to device characterization experiments and data analysis. D. N. contributed to the discussion of the results. V. P. conceived and supervised the project, designed the experiments, contributed to data analysis, and wrote the manuscript. All authors revised the manuscript.

### **Conflict of Interest**

The authors declare no conflict of interest.

### **Data Availability Statement**

The data that support the findings of this study are available from the corresponding author upon reasonable request.

### **References**

- [1] F. P. García De Arquer, A. Armin, P. Meredith, E. H. Sargent, *Nat. Rev. Mater.* **2017**, 2, 16100.
- [2] R. D. Jansen-van Vuuren, A. Armin, A. K. Pandey, P. L. Burn, P. Meredith, *Adv. Mater.* **2016**, 28, 4766.
- [3] J. Vanderspikken, W. Maes, K. Vandewal, *Adv. Funct. Mater.* **2021**, 31, 2104060.

- [4] R. D. J. Van Vuuren, J. M. Nunzi, S. N. Givigi, *IEEE Sens. J.* **2021**, *21*, 11339.
- [5] V. Pecunia, *Organic Narrowband Photodetectors: Materials, devices and applications*, IOP Publishing, Bristol, UK, **2020**.
- [6] K. J. Baeg, M. Binda, D. Natali, M. Caironi, Y. Y. Noh, *Adv. Mater.* **2013**, *25*, 4267.
- [7] V. Pecunia, *J. Phys. Mater.* **2019**, *2*, 042001.
- [8] K. Toyoda, *Digital Still Cameras at a Glance*, CRC Press, Boca Raton, USA, **2017**.
- [9] S. Aihara, H. Seo, M. Namba, T. Watabe, H. Ohtake, M. Kubota, N. Egami, T. Hiramatsu, T. Matsuda, M. Furuta, H. Nitta, T. Hirao, *IEEE Trans. Electron Devices* **2009**, *56*, 2570.
- [10] R. F. Lyon, P. M. Hubel, in *Final Progr. Proc. - IS T/SID Color Imaging Conf.*, Scottsdale, Arizona, **2002**.
- [11] R. Merrill, *US Pat.* 5,965,875, **1999**.
- [12] A. El Gamal, in *Dig. Int. Electron Devices Meet.*, IEEE, Stanford University, Stanford, **2002**.
- [13] T. Sakai, T. Takagi, K. Imamura, K. Mineo, H. Yakushiji, Y. Hashimoto, T. Aotake, Y. Sadamitsu, H. Sato, S. Aihara, *ACS Appl. Electron. Mater.* **2021**, *3*, 3085.
- [14] A. Altaqui, P. Sen, H. Schrickx, J. Rech, J.-W. Lee, M. Escuti, W. You, B. J. Kim, R. Kolbas, B. T. O'Connor, M. Kudenov, *Sci. Adv.* **2021**, *7*, DOI: 10.1126/sciadv.abe3196.
- [15] A. Altaqui, R. M. Kolbas, M. J. Escuti, B. T. O'Connor, M. W. Kudenov, *Appl. Opt.* **2021**, *60*, 2314.
- [16] V. Pecunia, D. Natali, M. Caironi, *Organic Photodetectors*, Elsevier, Amsterdam, The Netherlands, **2022**.
- [17] N. Strobel, M. Seiberlich, R. Eckstein, U. Lemmer, G. Hernandez-Sosa, *Flex. Print. Electron.* **2019**, *4*, 043001.
- [18] G. Pace, A. Grimoldi, M. Sampietro, D. Natali, M. Caironi, *Semicond. Sci. Technol.* **2015**, *30*, 104006.
- [19] S.-H. Lee, A. R. bin M. Yusoff, C. Lee, S. C. Yoon, Y.-Y. Noh, *Mater. Sci. Eng. R Reports* **2022**, *147*, 100660.
- [20] W. Qarony, H. A. Khan, M. I. Hossain, M. Kozawa, A. Salleo, J. Y. Hardeberg, H. Fujiwara, Y. H. Tsang, D. Knipp, *ACS Appl. Mater. Interfaces* **2022**, *14*, 11645.
- [21] C. Perumal Veeramalai, S. Feng, X. Zhang, S. V. N. Pammi, V. Pecunia, C. Li, *Photonics Res.* **2021**, *9*, 968.

- [22] S. Yakunin, Y. Shynkarenko, D. N. Dirin, I. Cherniukh, M. V Kovalenko, *NPG Asia Mater.* **2017**, *9*, e431.
- [23] J. Kim, C. Jo, M. Kim, G.-S. Park, T. J. Marks, A. Facchetti, S. K. Park, *Adv. Mater.* **2022**, *34*, e2106215.
- [24] W. Qarony, M. Kozawa, H. A. Khan, M. I. Hossain, A. Salleo, Y. H. Tsang, J. Y. Hardeberg, H. Fujiwara, D. Knipp, *Adv. Mater. Interfaces* **2020**, *7*, 2000459.
- [25] J. Gong, S. B. Darling, F. You, *Energy Environ. Sci.* **2015**, *8*, 1953.
- [26] V. Pecunia, L. G. Occhipinti, R. L. Z. Hoye, *Adv. Energy Mater.* **2021**, *11*, 2100698.
- [27] H. Seo, T. Sakai, H. Ohtake, M. Furuta, in *IEEE SENSORS 2014 Proc.*, IEEE, Valencia, Spain, **2014**.
- [28] T. Sakai, H. Seo, S. Aihara, H. Ohtake, M. Kubota, M. Furuta, in *Image Sensors Imaging Syst. 2014*, San Francisco, California, USA, **2014**.
- [29] T. Sakai, H. Seo, T. Takagi, M. Kubota, H. Ohtake, M. Furuta, in *2015 IEEE Int. Electron Devices Meet.*, IEEE, Washington, DC, USA, **2015**.
- [30] T. Takagi, H. Seo, T. Sakai, H. Ohtake, M. Furuta, *Electron. Imaging* **2016**, *28*, 1.
- [31] S.-J. Lim, D.-S. Leem, K.-B. Park, K.-S. Kim, S. Sul, K. Na, G. H. Lee, C.-J. Heo, K.-H. Lee, X. Bulliard, R.-I. Satoh, T. Yagi, T. Ro, D. Im, J. Jung, M. Lee, T.-Y. Lee, M. G. Han, Y. W. Jin, S. Lee, *Sci. Rep.* **2015**, *5*, 7708.
- [32] X. Bulliard, Y. W. Jin, G. H. Lee, S. Yun, D.-S. Leem, T. Ro, K.-B. Park, C.-J. Heo, R.-I. Satoh, T. Yagi, Y. S. Choi, S.-J. Lim, S. Lee, *J. Mater. Chem. C* **2016**, *4*, 1117.
- [33] M. G. Han, K. B. Park, X. Bulliard, G. H. Lee, S. Yun, D. S. Leem, C. J. Heo, T. Yagi, R. Sakurai, T. Ro, S. J. Lim, S. Sul, K. Na, J. Ahn, Y. W. Jin, S. Lee, *ACS Appl. Mater. Interfaces* **2016**, *8*, 26143.
- [34] G. H. Lee, X. Bulliard, S. Yun, D.-S. Leem, K.-B. Park, K.-H. Lee, C.-J. Heo, I.-S. Jung, J.-H. Kim, Y. S. Choi, S.-J. Lim, Y. W. Jin, *Opt. Express* **2019**, *27*, 25410.
- [35] H. Seo, S. Aihara, T. Watabe, H. Ohtake, M. Kubota, N. Egami, *Jpn. J. Appl. Phys.* **2007**, *46*, L1240.
- [36] H. Seo, S. Aihara, T. Watabe, H. Ohtake, T. Sakai, M. Kubota, N. Egami, T. Hiramatsu, T. Matsuda, M. Furuta, T. Hirao, *Jpn. J. Appl. Phys.* **2011**, *50*, 024103.
- [37] Y. Wang, B. Siegmund, Z. Tang, Z. Ma, J. Kublitski, S. Xing, V. C. Nikolis, S. Ullbrich, Y. Li, J. Benduhn, D. Spoltore, K. Vandewal, K. Leo, *Adv. Opt. Mater.* **2021**, *9*, 2001784.
- [38] F. Ullah, C.-C. Chen, W. C. H. Choy, *Adv. Energy Sustain. Res.* **2021**, *2*, 2000050.

- [39] P. E. Keivanidis, P. K. H. Ho, R. H. Friend, N. C. Greenham, *Adv. Funct. Mater.* **2010**, *20*, 3895.
- [40] R. L. Headrick, S. Wo, F. Sansoz, J. E. Anthony, *Appl. Phys. Lett.* **2008**, *92*, 063302.
- [41] Y. H. Huh, I.-G. Bae, H. G. Jeon, B. Park, *Opt. Express* **2016**, *24*, A1321.
- [42] K. Fostiropoulos, M. Vogel, B. Mertesacker, A. Weidinger, in *Org. Photovoltaics III* (Ed.: Z.H. Kafafi), **2003**, p. 1.
- [43] B. Friedel, P. E. Keivanidis, T. J. K. Brenner, A. Abrusci, C. R. McNeill, R. H. Friend, N. C. Greenham, *Macromolecules* **2009**, *42*, 6741.
- [44] M. Caironi, E. Gili, H. Sirringhaus, in *Org. Electron. II More Mater. Appl.*, Wiley, **2012**, pp. 281–326.
- [45] R. Hamilton, J. Smith, S. Ogier, M. Heeney, J. E. Anthony, I. McCulloch, J. Veres, D. D. C. Bradley, T. D. Anthopoulos, *Adv. Mater.* **2009**, *21*, 1166.
- [46] M. S. Vezie, S. Few, I. Meager, G. Pieridou, B. Dörfling, R. S. Ashraf, A. R. Goñi, H. Bronstein, I. McCulloch, S. C. Hayes, M. Campoy-Quiles, J. Nelson, *Nat. Mater.* **2016**, *15*, 746.
- [47] A. Sanzone, A. Calascibetta, M. Monti, S. Mattiello, M. Sassi, F. Corsini, G. Griffini, M. Sommer, L. Beverina, *ACS Macro Lett.* **2020**, *9*, 1167.
- [48] B. P. Parekh, A. A. Tangonan, S. S. Newaz, S. K. Sanduja, A. Q. Ashraf, R. Krishnamoorti, T. R. Lee, *Macromolecules* **2004**, *37*, 8883.
- [49] R. O’Shea, W. W. H. Wong, *Polym. Chem.* **2020**, *11*, 2831.
- [50] M. Moser, A. Wadsworth, N. Gasparini, I. McCulloch, *Adv. Energy Mater.* **2021**, *11*, 2100056.
- [51] R. Po, G. Bianchi, C. Carbonera, A. Pellegrino, *Macromolecules* **2015**, *48*, 453.
- [52] I. Riisness, M. J. Gordon, *Appl. Phys. Lett.* **2013**, *102*, 113302.
- [53] H. Hoppe, N. S. Sariciftci, *J. Mater. Res.* **2004**, *19*, 1924.
- [54] A. J. Ward, A. Ruseckas, I. D. W. Samuel, *J. Phys. Chem. C* **2012**, *116*, 23931.
- [55] A. Köhler, H. Bässler, *Electronic Processes in Organic Semiconductors: An Introduction*, Wiley-VCH Verlag GmbH & Co. KGaA, Weinheim, Germany, **2015**.
- [56] S. Zeiske, O. J. Sandberg, N. Zarrabi, W. Li, P. Meredith, A. Armin, *Nat. Commun.* **2021**, *12*, 3603.
- [57] R. H. Bube, S. A. Rice, *Photoconductivity of Solids*, John Wiley & Sons, New York, USA, **1960**.
- [58] A. Rose, *RCA Rev.* **1951**, *12*, 362.
- [59] Y. Fang, A. Armin, P. Meredith, J. Huang, *Nat. Photonics* **2019**, *13*, 1.

- [60] V. Pecunia, Y. Yuan, J. Zhao, K. Xia, Y. Wang, S. Duhm, L. Portilla, F. Li, *Nano-Micro Lett.* **2020**, *12*, 27.
- [61] T. N. Ng, W. S. Wong, M. L. Chabinye, S. Sambandan, R. A. Street, *Appl. Phys. Lett.* **2008**, *92*, 213303.
- [62] Y. Wang, X. Huang, T. Li, L. Li, X. Guo, P. Jiang, *Chem. Mater.* **2019**, *31*, 2212.
- [63] V. Pecunia, K. Banger, H. Sirringhaus, *Adv. Electron. Mater.* **2015**, *1*, 1400024.
- [64] K. J. Baeg, D. Khim, S. W. Jung, J. B. Koo, I. K. You, Y. C. Nah, D. Y. Kim, Y. Y. Noh, *ETRI J.* **2011**, *33*, 887.
- [65] A. M. Gaikwad, Y. Khan, A. E. Ostfeld, S. Pandya, S. Abraham, A. C. Arias, *Org. Electron.* **2016**, *30*, 18.
- [66] J. Chai, F. Lu, B. Li, D. Y. Kwok, *Langmuir* **2004**, *20*, 10919.
- [67] Z. Weng, S. C. Dixon, L. Y. Lee, C. J. Humphreys, I. Guiney, O. Fenwick, W. P. Gillin, *Adv. Opt. Mater.* **2022**, *10*, 2101675.
- [68] A. I. Hofmann, E. Cloutet, G. Hadziioannou, *Adv. Electron. Mater.* **2018**, *4*, 1700412.
- [69] Y. Zhang, S.-W. Ng, X. Lu, Z. Zheng, *Chem. Rev.* **2020**, *120*, 2049.
- [70] R. Roesch, K. R. Eberhardt, S. Engmann, G. Gobsch, H. Hoppe, *Sol. Energy Mater. Sol. Cells* **2013**, *117*, 59.
- [71] T. Yamanari, T. Taima, J. Sakai, J. Tsukamoto, Y. Yoshida, *Jpn. J. Appl. Phys.* **2010**, *49*, 01AC02.
- [72] H. Lei, M. Wang, Y. Hoshi, T. Uchida, S. Kobayashi, Y. Sawada, *Appl. Surf. Sci.* **2013**, *285*, 389.
- [73] H. Kanda, A. Uzum, A. K. Baranwal, T. A. N. Peiris, T. Umeyama, H. Imahori, H. Segawa, T. Miyasaka, S. Ito, *J. Phys. Chem. C* **2016**, *120*, 28441.
- [74] B. C. Huang, Y. J. Lin, *Appl. Phys. Lett.* **2011**, *99*, 113301.
- [75] V. Pecunia, K. Banger, A. Sou, H. Sirringhaus, *Org. Electron.* **2015**, *21*, 177.

## Supporting Information

### **Solution-Based Integration of Vertically Stacked Organic Photodetectors Toward Easy-To-Fabricate Filterless Multi-Color Light Sensors**

*Ting Zhao, Kai Xia, Dario Natali, Vincenzo Pecunia\**

T. Zhao, K. Xia

Jiangsu Key Laboratory for Carbon-Based Functional Materials & Devices, Institute of Functional Nano & Soft Materials, Joint International Research Laboratory of Carbon-Based Functional Materials and Devices, Soochow University, China

Prof. D. Natali

Department of Electronics, Information and Bioengineering, Politecnico di Milano, P.za L. da Vinci, 32 Milan, 20133 Italy

and

Center for Nano Science and Technology @Polimi, Istituto Italiano di Tecnologia, Via Pascoli 70/3, I-20133 Milano, Italy

Prof. V. Pecunia

School of Sustainable Energy Engineering, Simon Fraser University, 5118 - 10285 University Drive, Surrey, V3T 0N1, BC, Canada

E-mail: vincenzo\_pecunia@sfu.ca

**Keywords:** organic photodetectors, narrowband photodetectors, color sensing, vertically stacked photodetectors, Foveon-like architecture

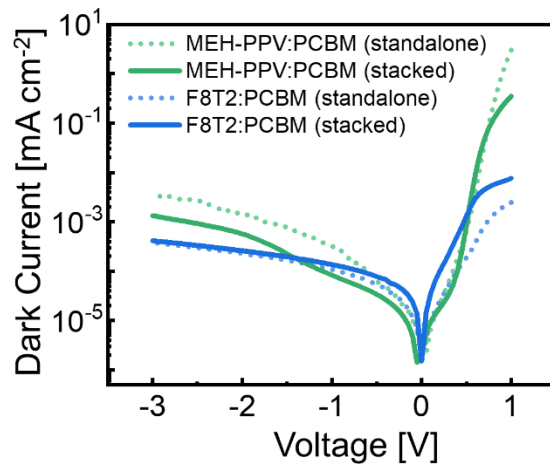


**Figure S1.** Dark current of F8T2:PCBM (1:1) and MEH-PPV:PCBM (1:4) photodetectors, both in their standalone and stacked configurations.

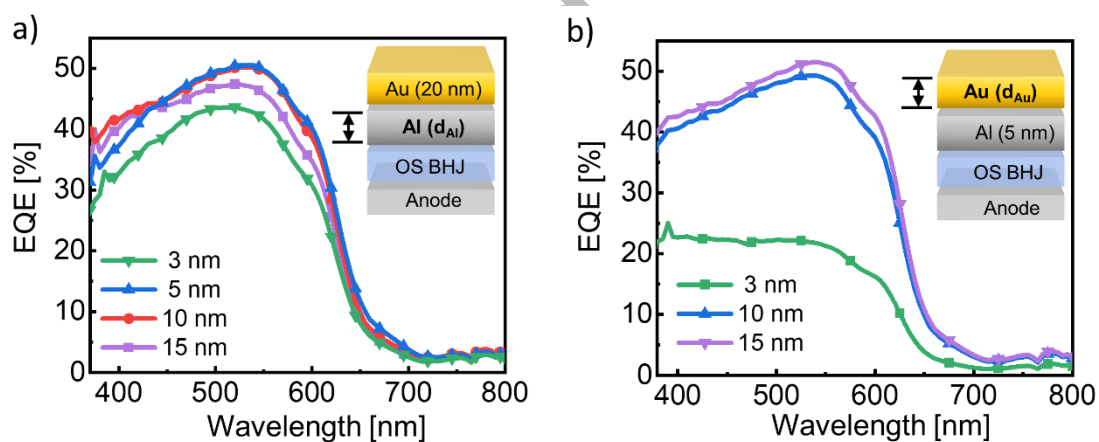


**Figure S2.** a) EQE spectra of reference organic photodetectors with different thicknesses of the aluminum electrode and a 5-nm-thick gold layer atop. b) EQE spectra of reference organic photodetectors with different thicknesses of the gold layer atop a 5-nm-thick aluminum layer.

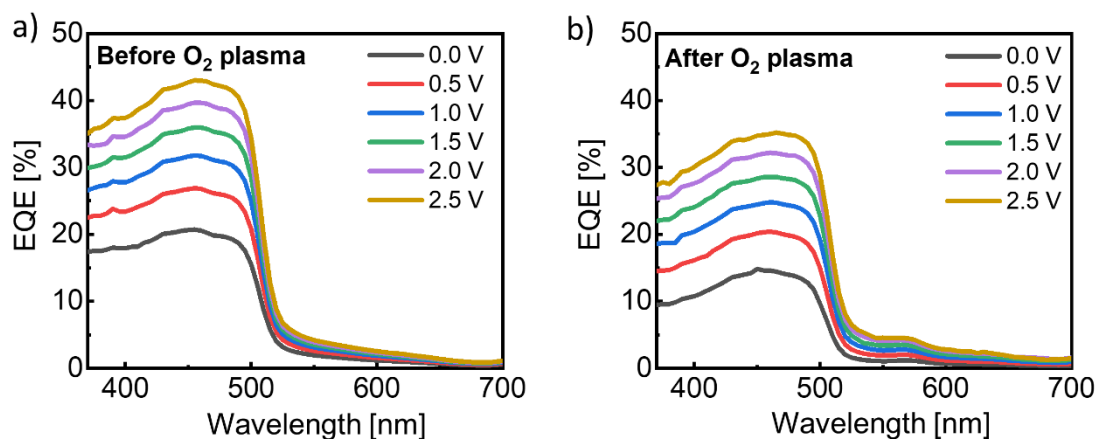


**Figure S3.** EQE spectra of an F8T2:PCBM photodetectors a) before and b) after the O<sub>2</sub> plasma treatment needed for the fabrication of vertically stacked photodetectors.

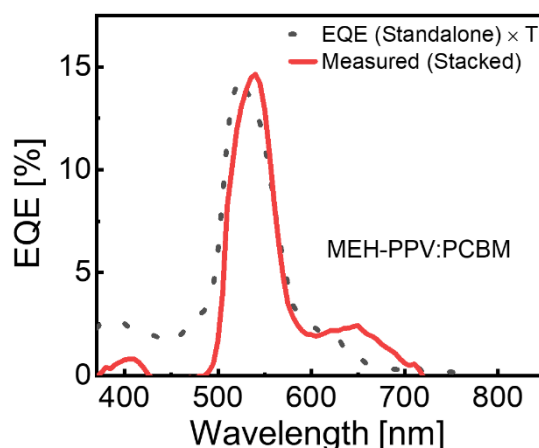


**Figure S4.** Comparison with the measured EQE spectrum of a stacked MEH-PPV:PCBM photodetector and the spectrum obtained by multiplying the EQE of a standalone MEH-PPV:PCBM with the transmittance (T) of the stack ITO | PEDOT:PSS | F8T2:PCBM | Al (5 nm) | Au (5 nm) | PMMA | Au (5 nm) (see the trace labeled ‘F8T2 PD | PMMA | Au (5nm)’ in Figure 5b, Main Text). Given the very good match between the two traces, we conclude that the lower EQE of the stacked MEH-PPV:PCBM devices can be traced to the transmittance of the specific electrode assemblies used, as opposed to the solution-based fabrication of the MEH-PPV:PCBM atop printable organic layers. This result points to the opportunity of integrating stacked organic photodetectors with higher apparent EQE through the adoption of emerging solutions for transparent electrodes, which hence constitute the worthwhile goal of future investigations.